PHOTONICS Research

Controllable two-dimensional Kerr and Raman–Kerr frequency combs in microbottle resonators with selectable dispersion

Xueying Jin,[1,3] Xin Xu,[1,4] Haoran Gao,[1] Keyi Wang,[2] Haojie Xia,[1] and Liandong Yu[1,*]

[1]School of Instrument Science and Opto-electronics Engineering, Hefei University of Technology, Hefei 230009, China
[2]Department of Precision Machinery and Precision Instrumentation, University of Science and Technology of China, Hefei 230026, China
[3]e-mail: xyjin007@hfut.edu.cn
[4]e-mail: xuxin@hfut.edu.cn
*Corresponding author: liandongyu@hfut.edu.cn

Received 27 August 2020; revised 25 November 2020; accepted 8 December 2020; posted 8 December 2020 (Doc. ID 408492); published 25 January 2021

We report a broadband two-dimensional (2D) Kerr and Raman–Kerr frequency comb generation in a silica bottle resonator accounting for azimuthal and axial degrees of freedom and pioneer a method that allows for controlled and reversible switching between a four wave mixing (FWM) state and a stimulated Raman scattering state. The repetition rate of the Raman–Kerr comb is not an integer number of the free spectral range, which spans more than 242 nm with hundreds of teeth. We show that, experimentally and numerically, multiple 2D comb regimes can be selectively accessed via dispersion engineering by exciting different orders of axial modes or modifying the curvature of the axial profile, involving cascaded FWM, Raman lasing, and Raman-assisted FWM. The effect of axial curvature on dispersion is associated with the axial mode number in bottle resonators. Our approach enables dispersion and spectral engineering flexibility in any resonator with localized axial modes.

https://doi.org/10.1364/PRJ.408492

1. INTRODUCTION

Optical frequency comb (OFC) generation in ultrahigh-Q whispering gallery mode (WGM) microcavities, denoted as microcombs [1,2], has attracted a broad spectrum of interests in science and technology, such as low-threshold microlasers, atomic clocks [3], and precision spectroscopy owing to their flexible repetition rate, wide bandwidth, and compact size. The exceptionally long photon lifetime (>1 μs) and small modal volume (V) enhance the light–matter interaction, which enables us to realize intracavity nonlinear frequency conversions with a low parametric oscillation threshold and broad bandwidth. In the case of a silica whispering gallery mode resonator (WGMR), the leading nonlinear effects, i.e., the third-order nonlinearities such as four-wave mixing (FWM), stimulated Raman scattering (SRS), and stimulated Brillouin scattering are observed and investigated [4,5]. In this regard, light–matter interaction in a continuous-wave (cw) pumped microcavity may initiate either a Kerr comb or Raman comb, as the Brillouin scattering frequency is more difficult to overlap with the resonant frequency. Specifically, the Kerr comb is related to Kerr nonlinearity induced optical parametric oscillation arising from the quasi-instantaneous electronic response of the medium to pump excitation; whereas the Raman comb, a fundamental inelastic scattering process, originates from the interaction between light and molecular vibrations. The interplay between the Kerr and Raman combs in microcavities has attracted great interest in recent years, and the application of SRS to comb generation has potential in fruitful fields such as Raman lasing [6,7], sensing, and self-frequency shift devices [2]. A central challenge in this area is selective excitation of the Kerr comb and Raman comb in a nonlinear WGM microcavity in regards to finding a convenient method to enhance or suppress the Raman process.

There have been promising efforts to achieve transitions between the Kerr comb state and the Raman oscillation state by designing the resonator size/free spectral range (FSR) [8,9], changing the pump power or laser-cavity detuning [10], adjusting the coupling gap [11], or optimizing the group velocity dispersion (GVD) through varying the wall thickness of bubble resonators [12]. However, geometrical control needs a high degree of controllability in the fabrication process, and the geometrical parameters are difficult to modify in practical applications once the microcavity is fabricated. As for silica microbottle resonators, the transition between a Kerr comb state and Raman oscillation state is more difficult due to their broad Raman line width and dense mode spectrum, compared to the

case in SiN, AlN, or silica microspheres. In this regard, alignment between the cavity resonance and the Stokes line may be impractical.

In this work, we present a convenient and simple approach to selectively accessing the parametric and/or Raman oscillation state without modification of resonator geometry based on the ultrahigh-Q silica microbottle platform. A controlled and reversible transition between modulation instability (MI) and Raman oscillation is realized by selectively exciting localized axial modes, designing the axial profile of the device, or adjusting the pump detuning. This Kerr–Raman competition is well described and analyzed by numerical simulations based on the generalized Lugiato–Lefever (L-L) equation, with the Raman effect included, which give important insights into the interplay between axial mode numbers and bottle axial curvature on dispersion. Moreover, wideband two-dimensional (2D) Kerr and Raman–Kerr frequency combs are experimentally demonstrated with a repetition rate smaller than one FSR. Our study provides a route for efficient Raman lasing and sensing applications in a silica microcavity and may be a critical step towards 2D frequency comb generation [13] in microcavity devices.

2. EXPERIMENTAL PRINCIPLE AND METHOD

Figure 1 describes the idea and generation principle of 2D Kerr combs and Raman combs in a silica microbottle, taking into account the azimuthal and axial mode families. In contrast to equatorial WGM resonators, light in a bottle resonator not only circulates circumferentially around the equator but also harmonically oscillates back and forth along the resonator axis between two "turning points," which are defined by an angular momentum barrier [14]. As seen in Fig. 1(a), the platform involves a coupling microfiber and a bottle microresonator. The microfiber was exploited to couple light in/out of the resonator and excite the frequency comb. In our device, both the parametric process (including degenerate FWM and non-degenerate FWM) and non-parametric process (SRS) exist in our bottle microresonator. SRS dominates when GVD is in the normal regime, since silica exhibits a large Raman gain bandwidth without the need of phase matching, while, in the anomalous GVD regime, FWM initiates before SRS due to its lower threshold. Experimentally, GVD is controlled by coupling the microfiber along the axis of the resonator [indicated by black arrow in Fig. 1(a)] or designing a proper axial profile and, therefore, achieving selective switching between the FWM-dominant state and SRS-dominant state. In particular, not only are the fundamental/azimuthal combs generated in the bottle, but also the axial comb lines can be created.

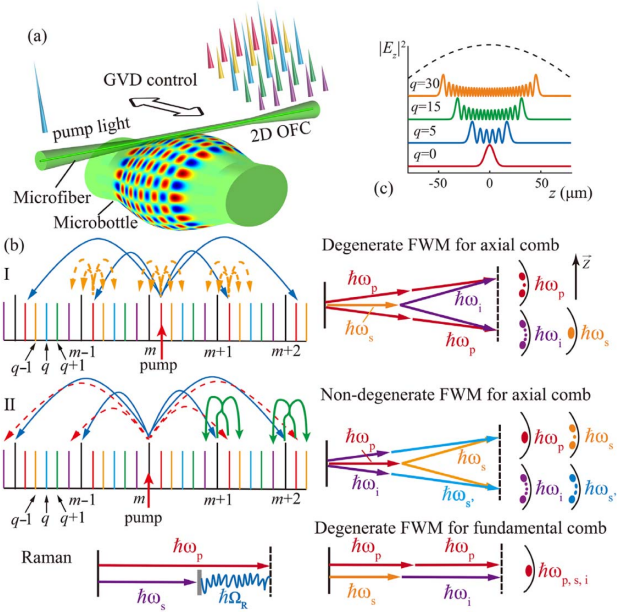

Fig. 1. Experimental method and principle of proposed device. (a) Illustration of tunable 2D frequency comb generation principle. The blue comb lines represent the fundamental combs, and the other comb lines indicate the axial combs. The black arrow denotes the GVD tailoring approach. (b) 2D wideband Kerr comb generation mechanisms of the FWM-based oscillation process with both axial and azimuthal modes involved. (I) Degenerate FWM oscillation for axial mode series; (II) non-degenerate FWM oscillation for axial mode series. Bottom: general principle for SRS and degenerate FWM for fundamental Kerr comb generation. (c) Characteristic axial field distributions of WGM powers in a bottle resonator.

We propose two mechanisms to generate 2D frequency combs: (i) by employing degenerate FWM only [method I in Fig. 1(b)] and (ii) by combining degenerate FWM and non-degenerate FWM [method II in Fig. 1(b)]. It is worth noting that the FWM for axial combs includes redistribution of photon momentum along the bottle axis (Z) in comparison to the fundamental comb case, which leads to different spatial distributions of comb modes. Routine FWM, including only the fundamental mode family, is also presented in the lower panel of Fig. 1(b) for comparison. It is seen that the mode fields are located in the vicinity of the equatorial plane of the resonator without the conversion of photon momentum along the resonator axis (Z) in the FWM process. Besides, the generation principle of SRS is also presented in the bottom left panel of Fig. 1(b). Figure 1(c) displays the axial distribution of the WGMs power for the quantum numbers $q = 0$, 5, 15, 30. The WGMs in the bottle resonator are characterized by three mode numbers (m, p, q), and m, p, and q indicate the azimuthal, radial, and axial quantum number, respectively. It is shown that this axial standing wave is greatly enhanced around the turning points of the harmonic motion. To effectively generate broadband 2D frequency combs, the axial mode eigenfrequencies have to match the azimuthal mode eigenfrequencies in a bottle resonator. Thus, the axial curvature should be carefully modified.

To make a high-Q bottle resonator with different geometrical parameters, a simple and convenient technique was employed by using a standard fiber fusion splicer (Fujikura FSM-80S) similar to the "soften-and-compress" method [15]. The single mode fiber (SMF) was first treated by the "heat-and-pull" technique with a hydrogen torch and then was cut off from the center. The microbottle was fabricated from controllably splicing together two sections of SMFs (Corning, SMF-28e) with a simple pretreatment on the fiber ends. The fabrication process contains four steps, as shown in Fig. 2. First, two normal stripped fibers were placed on two V-groove

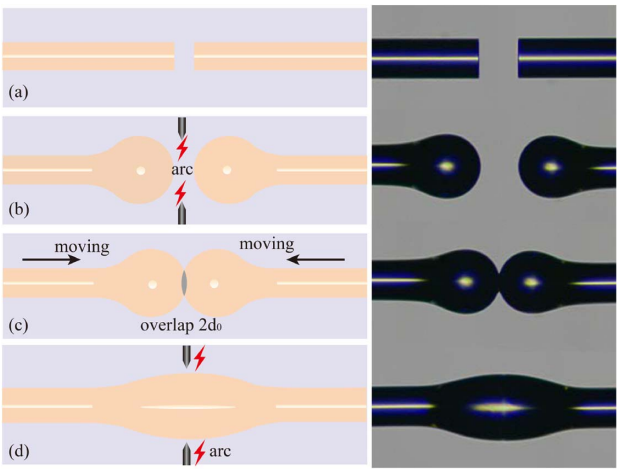

Fig. 2. Fabrication process of the microbottle resonators. The inset on the right indicates the microscopic images of the microbottle during the process.

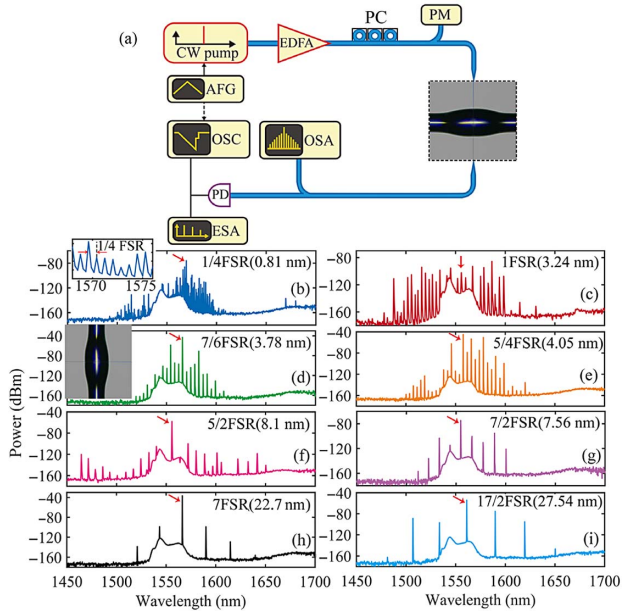

Fig. 3. (a) Experimental setup and device illustrating the optical frequency generation in bottle resonators. CW pump, continuous wave tunable pump source; EDFA, erbium-doped fiber amplifier; PC, polarization controller; PM, power meter; OSA, optical spectrum analyzer; ESA, signal and spectrum analyzer; OSC, digital storage oscilloscope; PD, photodetector; AFG, arbitrary function generator. (b)–(i) Experimental observation of eight primary Kerr combs exhibiting very different spacings of (b) 1/4-FSR$_m$, (c) 1-FSR$_m$, (d) 7/6-FSR$_m$, (e) 5/4-FSR$_m$, (f) 5/2-FSR$_m$, (g) 7/2-FSR$_m$, (h) 7-FSR$_m$, and (i) 17/2-FSR$_m$. The 2D Kerr comb spectrum is demonstrated in (a). The microfiber is placed at the bottle center [(d), inset] to excite the azimuthal and axial mode families.

clamps on the splicer. Then, the two fiber ends were softened by electrical arc discharge and reshaped into two spheres with smooth surfaces due to surface tension. Third, the left and right spheres move towards each other by driving motors of the splicer until a small overlap $2d_0$ was realized. Finally, we apply multiple short arcs with a duration of about 3 s to controllably soften the overlapping region. After the treatment, the bottle resonator was fabricated, which was caused by surface tension and material flow of fused silica. By this method, bottle resonators with different geometrical parameters (R_0, L, Δk) can be fabricated by controlling the size of the spheres on fiber ends, the number of arcs, and the overlapping region. We here prepared three bottle resonators (Device 1–Device 3) with different axial curvatures Δk but with approximately the same radius (~81.9 μm). The microbottle resonator fabricated by this method possesses Q factors up to 10^8 and large mode decoupling due to its prolate profile. Compared with the conventional "soften-and-compress" method, this approach generates a wider range of axial curvature (0.002–0.0075 μm^{-1}) and a larger bottle radius with good repeatability, allowing their use for generation of 2D frequency combs.

3. 2D KERR COMB GENERATION

The experimental setup, sketched in Fig. 3(a), is used for OFC generation with a microbottle resonator platform. The pump field from a cw pump laser (Toptica CTL 1550) with a linewidth smaller than 10 kHz is amplified by an erbium-doped fiber amplifier (EDFA) and, after passing a polarization controller (PC), is then launched into a bottle resonator to excite the OFC. We employed a power meter (PM) to monitor the optical power injected into the resonator. The polarization state of light was adjusted and stabilized by the PC. We selectively excited the axial modes as well as the coupling efficiency by vertically scanning the microfiber along the bottle axis. Afterwards, the output light from the microfiber is split into two paths. One was sent to an optical spectrum analyzer (OSA, Anritsu MS9740A), and the other was routed to a photodetector (PD, Thorlabs PDA05CF2) followed by an oscilloscope (Keysight DSO 4054A). The comb spectrum is also fed to a signal and spectrum analyzer (ESA, R&S FSW26) to monitor the corresponding RF spectra.

To generate wideband 2D Kerr combs, the microfiber was firstly excited at the center of a bottle resonator with $R_0 = 81.9$ μm, $L = 428.6$ μm, and $\Delta k = 0.003056$ μm^{-1}, as shown in Fig. 3. In this case, both of the basic mode and axial mode sequences can be excited [16,17] under an anomalous regime (see Section 4 for theoretical verification). The shape of the microbottle was fitted with parabolic profile $R_z \approx R_0[1 - (\Delta k z)^2/2]$, where R_0 is the maximal radius at $z = 0$, and Δk indicates the axial curvature of the profile. We adjusted the cavity loading by scanning the coupling microfiber along the bottle axis, measured the parametric oscillation threshold, and finely tuned the pump wavelength so that the pump can be self-thermally locked to a certain WGM. During the measurement process, the coupling microfiber was always in physical contact with the bottle resonator to ensure the coupling stability. Figure 3 presents the measured transmitted optical spectra for the different identified Kerr comb patterns, corresponding to 1/4-FSR$_m$, 1-FSR$_m$, 7/6-FSR$_m$, 5/4-FSR$_m$, 5/2-FSR$_m$, 7/2-FSR$_m$, 7-FSR$_m$, and 17/2-FSR$_m$ of the bottle resonator, respectively. Here, FSR$_m$ is the azimuthal FSR of the resonator. The "Type I" [18] fundamental comb with sidebands separated

by one azimuthal FSR was realized [Fig. 3(c)], and, by tuning the pump wavelength, the "Type II" comb with multimode spaced lines was also verified [Fig. 3(h)]. It is seen from Fig. 3(c) that the first-order signal–idler photons are symmetrically located with respect to the pump with the spacing of 3.24 nm, which is in good agreement with the calculated FSR_m [$\mathrm{FSR}_m \approx \lambda^2/(2\pi n R_0) = 3.241$ nm]. Different primary comb spacings use the same pump power, since different radial mode families are excited simultaneously in the resonator, and the energy conservation condition is met for these modes. The detuning between the pump and resonance may induce the variations of comb spacing, but the effect is limited owing to the on-resonance requirement. In our experiment, we observed a ratio of less than two when changing the detuning parameter. Thus, the geometrical dispersion difference is responsible for this observation. We attribute the above two types of fundamental combs to degenerate FWM [lower right panel of Fig. 1(b)], as no Raman oscillation signal is observed. Note that the pump wavelengths in Fig. 3 are larger than the zero dispersion wavelength (ZDW) of Bottle 1 [1531 nm see Section 5] and thus correspond to the anomalous dispersion regime for $q = 0$.

It is interesting to find that the repetition rate of the comb is not an integral multiple of the fundamental FSR in some cases, as shown in Figs. 3(d)–3(g), 3(i), and 3(b). For example, in Fig. 3(b), a broadband comb spaced by $1/4\text{-FSR}_m$ can be generated, which is simultaneously initiated at the axial and azimuthal eigenfrequencies. The low repetition frequency axial comb lines match a series of equidistant axial eigenfrequencies and are localized between adjacent azimuthal comb series. The FSR of the wideband azimuthal mode series is exactly four times the FSR of the narrowband axial mode series [$\mathrm{FSR}_m/\mathrm{FSR}_q = 3.24\ \mathrm{nm}/0.81\ \mathrm{nm} = 4$, the calculated value $\mathrm{FSR}_q \approx \lambda^2\Delta k/(2\pi n) = 0.811$ nm]. Such a comb is termed a 2D frequency comb by taking into account dynamics in the azimuthal and axial directions with different orbital momenta, which was theoretically predicted in Refs. [13,19]. Additionally, the frequency comb with $5/4\text{-FSR}_m$ spacing is also excited by degenerate FWM [Fig. 3(e)]. Therefore, the generation of $1/4\text{-FSR}_m$ comb lines may be ascribed to the cascaded non-degenerate FWM between the 1-FSR_m mode series and the $5/4\text{-FSR}_m$ series [mechanism II in Fig. 1(b)]. Besides the $1/4\text{-FSR}_m$ and its integer multiples mode series, there is also the $7/6\text{-FSR}_m$ series that is excited, as shown in Fig. 3(d). This may be explained similar to the case of the $5/4\text{-FSR}_m$ series, but belongs to the family of modes with different radial quantum number p.

4. DISPERSION ENGINEERING AND CONTROLLED RAMAN–KERR TRANSITION

We then investigate the dispersion engineering by selective exciting of axial modes or designing the axial profile of the device

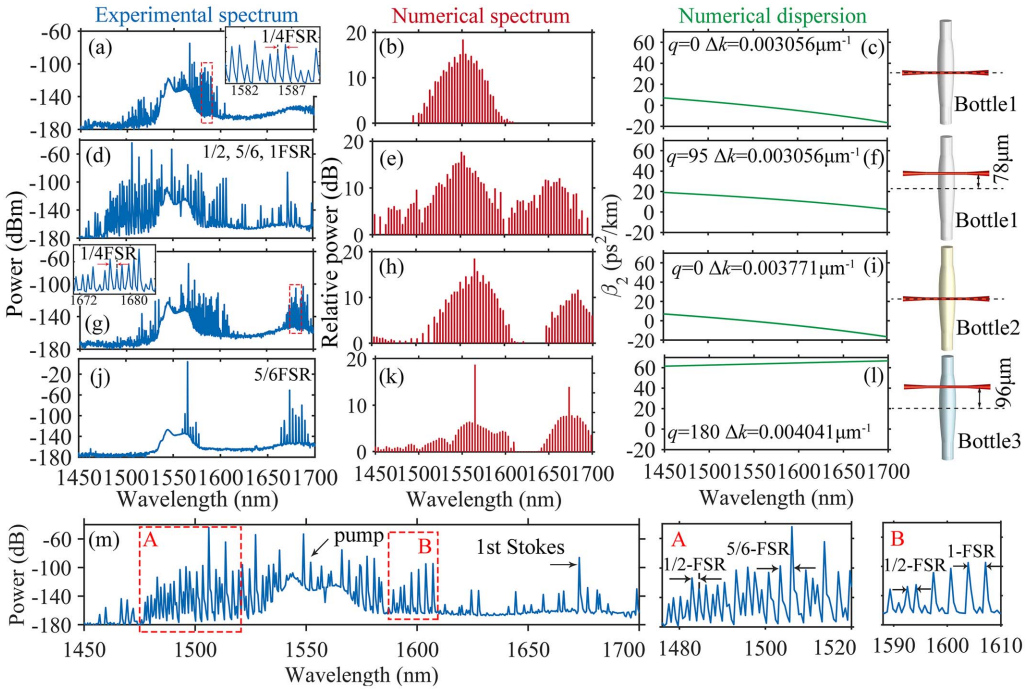

Fig. 4. Comparison between experimental and simulated spectra along with the GVD dispersion curves: dispersion engineering and controllable Raman–Kerr transition. (a)–(c) The 2D Kerr combs excitation in the anomalous dispersion regime when the silica bottle resonator (Device 1, $\Delta k = 0.003056\ \mu\mathrm{m}^{-1}$) was excited at the center. (d)–(f) Raman–Kerr comb excitation in the weak normal dispersion regime when the silica bottle resonator (Device 1) was excited at 78 μm from center. (g)–(i) Raman–Kerr comb excitation in the anomalous dispersion regime when the silica bottle resonator (Device 2, $\Delta k = 0.003771\ \mu\mathrm{m}^{-1}$) was excited at the bottle center. (j)–(l) Raman lasing excitation in the strongly normal dispersion regime when the silica bottle resonator (Device 3, $\Delta k = 0.004041\ \mu\mathrm{m}^{-1}$) was excited at 96 μm from center. Corresponding numerical simulation for (b), (e), (h), and (k) with the same detuning $\delta = -5.4 \times 10^{-8}$. (m) Magnified view of aperiodic hyperparametrical oscillations observed in (d). Inset A: magnified view of the comb spectrum from 1476 to 1520 nm. Inset B: magnified view of the comb spectrum from 1588 to 1610 nm. The peak widths of the comb lines are limited by the resolution and sampling points of the OSA.

and demonstrate that a controlled deterministic transition between Kerr combs and Raman oscillation can be achieved in our microbottle-taper coupling system. In our experiment, Raman–Kerr combs are generated in three silica bottle resonators (Device 1–Device 3). The three microresonators have the same radius (~81.9 μm) but with different axial curvatures Δk. We excited different orders of axial modes by changing the microfiber axial position and measured the comb spectra with nearly zero pump detuning. Figures 4(a) and 4(d) describe two distinct regimes of operation by selective excitation of different orders of axial modes. The pump power was always fixed at 300 mW, and the mode selection has been changed by scanning the coupling fiber along the resonator axis [17]. Figure 4(a) shows cascaded FWM combs with 1/4-FSR axial modes when the microfiber was coupled at the bottle center so that it falls into the anomalous regime. To demonstrate the GVD adjustment based on the coupling position, the microfiber was moved 78 μm away from the bottle center of Device 1 ($q = 95$, $\Delta k = 0.003056\ \mu m^{-1}$). This position was monitored by a CCD camera above the coupling regime. Figure 4(d) presents aperiodic wideband hyperparametric oscillation under weak normal dispersion [Fig. 4(f)]. Different FWM oscillations as well as SRS family modes are initiated: the FWM photon pairs around the pump and 1600 nm are separated by 1-FSR (basic mode sequence); 5/6-FSR and 1/2-FSR mode families are also observed in the vicinity of ~1506 nm and 1483 nm, respectively [see Fig. 4(m) for hyperparametric oscillation details]. The peak located at 1673.02 nm indicates the SRS line, with a Stokes shift of ~13 THz from the pump. These axial modes have a large spatial overlap and interaction among them, leading to different frequency spacing and, hence, an asymmetric spectrum [20]. It is noteworthy that the generated comb lines are stronger than the pump in this case. This can be ascribed to the fact that higher power transferring to the combs could put the pump effectively into the under-coupled regime, and, hence, the pump transmission may decrease or even exhibit a dip [see Fig. 4(m)]. Additionally, the spectra on the anti-Stokes side are denser than on the Stokes side, which is similar to the results obtained in Ref. [21]. We attributed it to the increase of probability for FWM oscillation on the blue side of the spectrum due to higher Q factors and larger WGM density. Another peculiarity of this frequency comb is the significant asymmetry in the signal and idler sidebands. For example, in Fig. 4(m) close to the pump, the idler photon (at 1548.8 nm) is much stronger than the signal photon (at 1555.3 nm). We may ascribe this phenomenon to the high modal density of the bottle microresonator. Experimentally, the laser usually pumps a mode cluster (not a single mode), which involves several degenerate modes. Each mode sequence with slightly different geometrical dispersion has its own parametric oscillation. Yet, the signals and idlers generated by these oscillations have nearly the same frequency, and, thus, they can interfere with each other. Consequently, this interference may suppress either the signal light or idler light, leading to the asymmetry of the comb spectrum.

Figure 4(g) shows a Raman-assisted Kerr comb with an identical spacing of 1/4-FSR. It was realized by switching to another bottle resonator with a different axial profile (Device 2, $\Delta k = 0.003771\ \mu m^{-1}$) for pumping. This broadband spectrum is formed by the initial Raman scattering and the subsequent non-degenerate FWM process. The SRS has a broad bandwidth gain of more than 40 THz in silica, which is much larger than FSR_m (0.40 THz) and FSR_q (0.10 THz) of the bottle resonator. As a result, more than 86 Kerr comb lines arise near the pump, and 29 Raman comb lines occur in the Raman waveband. We found that the Stokes components are not a single Raman lasing but a series of comb lines spaced by one FSR_q [left inset in Fig. 4(g)]. To the best of our knowledge, this is the first experimental observation of a 2D Raman–Kerr comb that simultaneously excites the axial and azimuthal components. One expects that the transition process is determined by the cavity GVD, circulating power (pump detuning), and polarization state of the pumped mode. For low q modes, variation of Δk has little influence on the cavity dispersion [Figs. 4(c) and 4(i)]. Thus, the transition from an FWM state to a Raman–Kerr state in Fig. 4(g) may be explained by the excitation of modes with different polarizations [10]. By further excitation of higher-order axial modes $q = 180$ in a bottle with more pronounced axial profile (Device 3, $\Delta k = 0.004041\ \mu m^{-1}$), we also observed Raman lasing in a strongly normal GVD regime. Figure 4(j) describes a multimode Raman lasing spectrum with nearly no FWM, which verifies a simple and convenient method for mode dispersion management. Note that the changing of axial profile Δk works only for large axial mode numbers q (see Section 5 for detail). Figure 4 offers

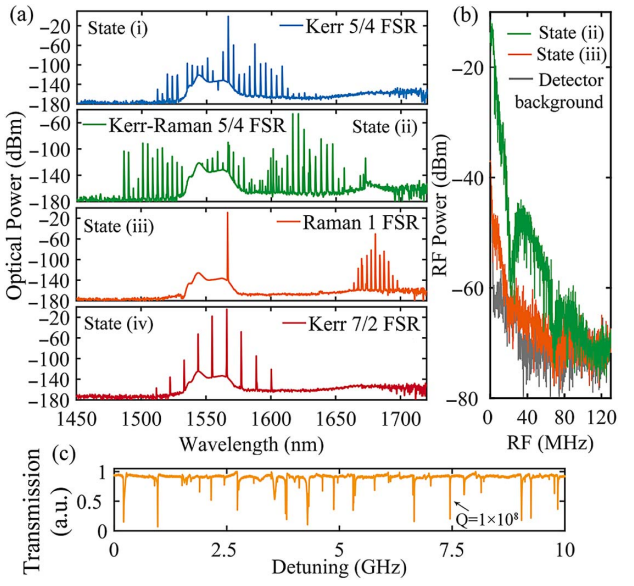

Fig. 5. (a) Transition between FWM oscillation and Raman oscillation in a bottle resonator with decreasing pump detuning from top to bottom. State (i): when the pump is largely blue-detuned, the Kerr comb with 5/4-FSR spacing is obtained; state (ii): when the detuning is decreased, the Kerr comb broadens, and the single Raman line starts; state (iii): when the pump is further decreased, the Kerr comb lines disappear, and only the Raman-assisted comb exists; state (iv): when the detuning is at its smallest, the Raman comb vanishes, and a 7/2-FSR Kerr comb starts. (b) RF spectra corresponding to state (ii) and state (iv) in (a). (c) Transmission measurement of the bottle resonator at ~1567 nm. The laser is tuned into the resonance with an increasing wavelength.

insightful understanding of the GVD effect on the formation of Raman–Kerr combs. Our results suggest that three distinct regimes can be selectively accessed via dispersion engineering by excitation of different axial modes, designing a proper axial profile, as well as adjusting the polarization state.

Next, we explore the pump detuning dependency. Figure 5(a) shows the Kerr–Raman transition process for a decreased blue detuning of the pump. By tuning the pump ($P_{\mathrm{in}} = 300$ mW) from a short to a long wavelength, a stable Kerr oscillation with 5/4-FSR spacing is firstly generated [state (i)]. We perform in the effective blue-detuned region, where the spectrum is thermally stable [22]. Hence, it can be regarded as a Turing pattern comb in the case of axial modes. The exhibited 5/4-FSR spacing characteristics originate from the axial components of modes with the same axial but different azimuthal quantum numbers. Then, we slightly decreased the detuning of the pump and obtained a broadband spectrum [state (ii)]. The occurrence of a broader spectrum is ascribed to stronger coupling of pump light into the cavity resonance and the subsequent additional cascaded FWM peaks based on degenerate and non-degenerate processes. Meanwhile, a 5/4-FSR Kerr comb converts into a Raman–Kerr comb with the same frequency spacing. The non-equidistant comb lines in the vicinity of 1600 nm are caused by the coupling between different transverse modes. By further decreasing the detuning, we observed a distinct behavior where the Kerr comb disappeared and SRS comb (Raman shift ∼12.9 THz) started, which is an indication of a Raman-dominant state [state (iii)]. There are no multiple overlapped comb lines for this Raman-assisted Kerr state, indicating that the Stokes and adjacent FWM components are supposed to arise from the same mode family (fundamental mode family), and the modal overlap is practically negligible in this case. When the detuning is at its smallest, the SRS comb disappeared, and a 7/2-FSR Kerr comb reappeared [state (iv)]. We observed a reduction in the RF noise from state (ii) to state (iii), as shown in Fig. 5(b), which implies that the low-noise state may be affected by Raman oscillation. The comparable high RF noise in state (ii) suggests the loss of the mode-locked state for the Kerr–Raman comb. Figure 5(c) displays the typical transmission spectrum of the bottle resonator, where a resonance mode with a high-Q factor up to $\sim 1 \times 10^8$ is presented. The laser was scanned until the selected high-Q mode was excited. Compared to previous work where a 2-FSR comb at the fundamental mode sequence is generated in this case [9], a silica bottle platform here provides much more flexibility in its repetition rate. In summary, we demonstrated controllable switching from FWM to the Raman state and then back to the FWM state. The experimental results are in good agreement with the following simulation results.

5. THEORETICAL MODEL AND SIMULATION

To gain more physical insight into the tunable Raman–Kerr combs generated in bottle resonators, we analyzed the dispersion engineering and Kerr–Raman transition process utilizing our theoretical models. Kerr combs initiated in a bottle resonator mainly involve two different families of WGMs: the azimuthal mode series with spacing of one FSR, $\mathrm{FSR}_m = f_m - f_{m-1}$, and the axial mode series with $\mathrm{FSR}_q = f_q - f_{q-1}$ spacing. Here, we focus on the dispersion tailoring based on these longitudinal FSR spaced WGMs. The total dispersion in a bottle resonator consists of two contributions: that is the material dispersion $\Delta\mathrm{FSR}^{\mathrm{M}}$ and geometry dispersion $\Delta\mathrm{FSR}^{\mathrm{G}}$. The geometrical dispersion is interpreted as the variation of the FSR and can be calculated via an approximation of the eigenfrequencies of bottle resonators. The resonance frequency f_m of bottle microresonator modes with a harmonic profile is given by [23]

$$f_m = \frac{c}{2\pi n}\left[\left(\frac{U_{mp}}{R_0}\right)^2 + \left(q + \frac{1}{2}\right)\Delta E_m\right]^{1/2}, \tag{1}$$

where $U_{mp} = m + \alpha_p (m/2)^{1/3} + (3/20)\alpha_p^2 (m/2)^{-1/3}$, α_p is the pth root of the Airy function for different radial modes, which is equal to 2.338, 4.088, and 5.521 for $p = 1, 2, 3$, respectively, and $\Delta E_m = 2U_{mp}\Delta k / R_0$. Δk and R_0 indicate the axial curvature and maximum radius of a bottle resonator. m is the azimuthal mode number, and q denotes the axial mode number. c is the speed of light in vacuum, and n denotes the refractive index of the material. Hence, the FSR and geometrical dispersion can be calculated from the resonator eigenfrequencies f_m as follows [24]:

$$\begin{aligned} \mathrm{FSR} &= f_m - f_{m-1}, \\ \Delta\mathrm{FSR}^{\mathrm{G}} &= (f_{m+1} - f_m) - (f_m - f_{m-1}). \end{aligned} \tag{2}$$

On the other hand, the material dispersion is proportional to the material GVD and can be expressed as $\Delta\mathrm{FSR}^{\mathrm{M}} \approx [c^2\lambda^2/(4\pi^2 n^3 R_0^2)] \cdot \mathrm{GVD}$; here, $\mathrm{GVD} = -(\lambda/c)(\partial^2 n/\partial\lambda^2)$, which can be solved numerically by exploiting the Sellmeier equations. The total dispersion, which takes into account geometrical dispersion as well as material dispersion, can therefore be expressed as

$$\Delta\mathrm{FSR} = \Delta\mathrm{FSR}^{\mathrm{M}} + \Delta\mathrm{FSR}^{\mathrm{G}}. \tag{3}$$

We then converted ΔFSR into the widely used second-order dispersion β_2 by applying the approximated expression [25]

$$\beta_2 = -\frac{1}{4\pi^2 R_0} \cdot \frac{\Delta\mathrm{FSR}}{\mathrm{FSR}^3}\ [\mathrm{ps}^2/\mathrm{km}]. \tag{4}$$

Figure 6(a) shows the calculated total dispersion ΔFSR as a function of wavelength for silica bottle resonators with axial mode number $q = 0$. We study three bottles with different maximum radii of $D_1 = 163.8$ μm, $D_2 = 185.6$ μm, and $D_3 = 200$ μm. Larger diameters offer a flattening of the dependence of FSR on the wavelength. Specifically, the dispersion of sample 1 increases from −2.16 to 3.51 MHz within the waveband of 1.4–1.7 μm, whereas, for sample 2 and sample 3, this value changes from −1.40 to 3.10 MHz and −1.07 to 2.83 MHz, respectively. The flat dispersion is critical for a wideband frequency comb generation. Additionally, the ZDW shifts to a shorter wavelength with an increased diameter [see inset in Fig. 6(a)]. Figure 6(b) plots the dispersion for different dimensions of bottle resonators at a wavelength of 1550 nm. It is seen that larger bottle sizes increase the dispersion for a fixed q. For fundamental mode family $q = 0$, the anomalous dispersion occurs when the size of the resonator exceeds 75 μm. At the radius of 81.9 μm [vertical black dashed line in Fig. 6(b), Device 1], the total dispersion for $q = 0$ and

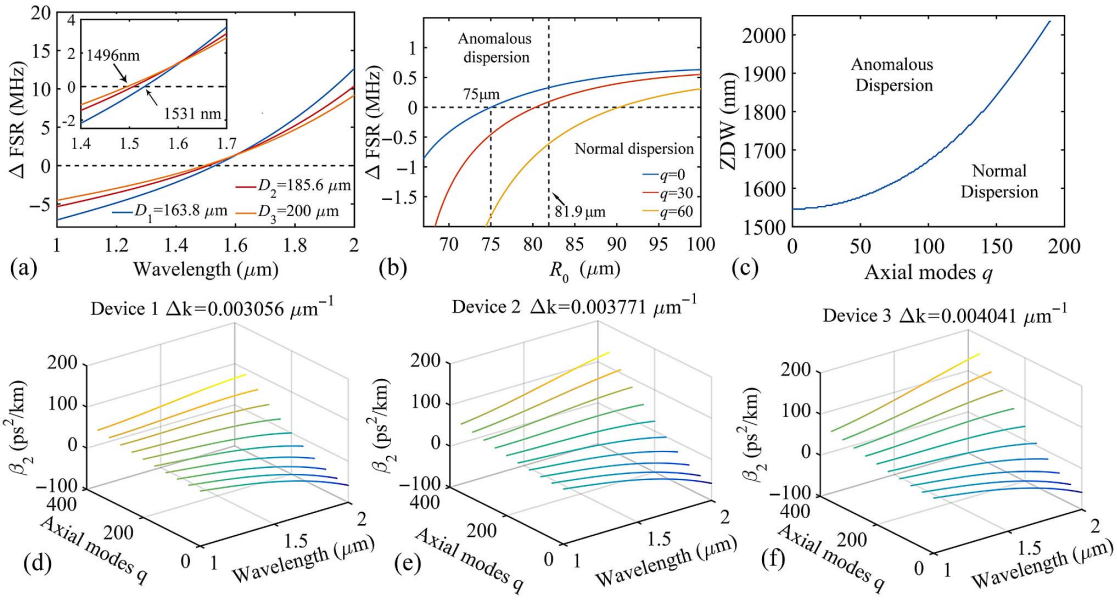

Fig. 6. (a) Calculated dispersion of silica bottle microresonators with fundamental modes $q = 0$ for three different resonator radii. (b) Dispersion versus the maximum radius of the microbottle resonator for different axial modes $q = 0$, $q = 30$, and $q = 60$. (c) Calculated ZDW of sample 1 as a function of axial mode numbers q. (d)–(f) Dispersion curves as a function of axial modes q and wavelength for different axial curvatures (d) $\Delta k = 0.003056$ μm^{-1}, (e) $\Delta k = 0.003771$ μm^{-1}, and (f) $\Delta k = 0.004041$ μm^{-1}.

$q = 30$ is in the anomalous regime (ΔFSR > 0), while for $q = 60$ is in the normal dispersion regime (ΔFSR < 0). This provides a convenient and flexible scheme for dispersion and ZDW adjustment without modifying the resonator geometry. Experimentally, this can be implemented simply by adjusting the axial coupling positions of the microfiber. For example, the fundamental mode $q = 0$ is excited when the coupling fiber is positioned at $z = 0$, and the axial mode $q = 30$ can be initiated when the microfiber is moved 45.2 μm away from the center (at the caustic of bottle modes), which can be obtained by calculating axial mode field distributions of the bottle resonator [17]. Indeed, to ensure that the 2D modes, including the azimuthal and axial series, are excited in the bottle, the central excitation position is preferable. To further confirm the GVD adjustment depending on axial mode number q, we provided the calculated ZDW when q is increased from 0 to 190, as shown in Fig. 6(c). Specifically, ZDW alters from 1531 to 1809 nm with an increase of q from 0 to 150, suggesting a simple and large-scale ZDW and GVD engineering approach. This interesting characteristic may push the ZDW of silica towards the mid-infrared (mid-IR) range and is favorable for broadband Kerr comb generation in this waveband.

We next study the relationship between GVD and resonator axial curvature Δk and demonstrate an additional degree of freedom to control the dispersion in bottle resonators. Figures 6(d)–6(f) show the calculated dispersion for three bottles with different axial curvatures (Devices 1–3) but approximately the same radii as a function of axial mode number q and wavelength. It is found that the GVD does not change significantly for smaller q modes. Nevertheless, for higher q modes, the dispersion becomes larger with an increased Δk. There exists a point (by selecting an appropriate axial mode q) at which the bottle exhibits a weak flattened normal dispersion, and the GVD value at this point can be tuned by choosing the bottle axial profile. From the above discussions, we can conclude that the total dispersion in a bottle resonator can be managed by selecting different axial modes and axial profile curvatures, and the interplay between these two effects should be considered. Compared to the dispersion control method in the microbubble [26], which can be realized by designing the diameter and wall thickness, the bottle resonator provides a post fabrication dispersion management scheme without changing the resonator geometry.

Based on the above dispersion analysis, we introduce the generalized L-L equation, with SRS taken into account, to model and analyze the Kerr–Raman transition dynamics. The generalized L-L equation is given as

$$\left(t_R\frac{\partial}{\partial t}+\frac{\alpha+\theta}{2}+i\delta+i\frac{\beta_2 L}{2}\frac{\partial^2}{\partial\tau^2}\right)E-i(1-f_R)\gamma L|E|^2E$$
$$-if_R\gamma L\left[E\int_{-\infty}^{\tau}h_R(\tau-\tau')|E|^2\mathrm{d}\tau'\right]-\sqrt{\theta}E_{\mathrm{in}}=0. \quad (5)$$

The second and third terms on the left side describe the Kerr and Raman effects, respectively. Here, E is the envelope of the intracavity field, t and τ are the slow time and fast time, respectively, t_R refers to the roundtrip time, L is the cavity length, α and θ indicate the intrinsic loss and external coupling coefficient, respectively, δ accounts for the pump phase detuning, β_2 represents the GVD, γ denotes the nonlinear coefficient, and $|E_{\mathrm{in}}|^2$ refers to the pump power. f_R is the Raman fractional response for silica, $f_R = 0.18$, and $h_R(\tau)$ indicates the Raman response function. In our simulations, the Raman effect is calculated in the frequency domain with a Lorentzian lineshape of central frequency $\Omega_R = -13$ THz and bandwidth $\Delta\Omega_R = 40$ THz [27]. To simulate the experimentally exploited device,

we choose $t_R = 2.49$ ps, $L = 2\pi \times 81.9$ μm, $\alpha = 4.3 \times 10^{-6}$, $\theta = 1.4 \times 10^{-6}$, $\gamma = n_2\omega_0/(cA_{\text{eff}}) \approx 0.0060$ W$^{-1}\cdot$m^{-1}, and $|E_{\text{in}}|^2 = 1$ mW. Numerical simulations were performed by solving Eq. (5) with split-step Fourier algorithm [28]. The wavelength-dependent dispersion is taken into account within the Fourier term. The GVD curves on the right column of Fig. 4 were calculated by solving Eqs. (1)–(4) and extracted from Figs. 6(d)–6(f).

Figure 4 (second and third columns) shows the simulation results of multiple different regimes involving the Kerr comb, Raman–Kerr comb, and Raman comb generation. The switching between three distinct regimes was realized via dispersion engineering just by adjusting the coupling positions of the microfiber along the bottle axis or choosing different axial curvatures. We first excited Device 1 ($\Delta k = 0.003056$ μm^{-1}) at the bottle center, which exhibits a weak anomalous dispersion. As seen in Fig. 4(b), a stable Kerr comb spectrum appears as we expected. This corresponds to a Turing pattern regime or primary comb [29], which originates from the cascaded FWM process at a 1-FSR spacing. Note that no Raman comb lines were observed, suggesting that the FWM comb is dominant in this state. Then, we moved the coupling microfiber 78 μm away from the bottle center and observed the output spectrum [Fig. 4(e)]. The excitation of the $q = 95$ axial mode pushes the resonator to a weak normal dispersion regime. It is found that both Kerr and Raman combs are simultaneously excited in this regime. Next, we switched to a bottle resonator with larger axial curvature (Device 2, $\Delta k = 0.003771$ μm^{-1}) and excited it at the bottle center ($q = 0$). Figure 4(h) displays a spectrum where Raman-assisted non-degenerate FWM has been initiated in the resonator. It was realized by pumping another WGM resonance with a different polarization state [6]. The results further confirm that both Kerr and Raman effects can be generated under anomalous dispersion once the pump power exceeds the Raman threshold. Distinct from the weak normal GVD case, the Raman oscillation without FWM is observed in simulations with a strongly normal dispersion regime. This was generated when Device 3 ($\Delta k = 0.004041$ μm^{-1}) was excited at 96 μm away from the bottle center [Fig. 4(l)]. No appreciable Kerr combs were excited, and strong Raman lines were created at a frequency of ∼13 THz red shifted from the pump. The absence of the Kerr comb in this case is the result of the strongly normal GVD, therefore rendering a negligible MI gain [30]. The Kerr–Raman transition behavior revealed by simulations is similar to our experimental observations. The differences between the experimental results and numerical results can be explained by the following two main reasons. First, the Q factor and the WGM density are different for various modes, thereby rendering different probabilities of optimal conditions for FWM oscillation in different modes. Second, mode coupling between different mode families and additional device loss in the system could increase the loss in our experiment. Our numerical results further confirm the feasibility of the dispersion management method in our bottle resonators.

Widely known, the transition between Kerr and Raman combs depends on the gain competition between the MI and Raman gain in WGM microcavities [8,9]. In contrast to the MI gain spectrum in an optical fiber [31], the MI gain in the cavity system has a discrete density-of-state and is absent adjacent to the pump. As a result, with an increase of input power, the MI gain spectrum may shift away from the pump due to the variations of the phase-mismatching term [32]. Nevertheless, the Raman gain in a silica cavity has a broadband spectrum that spans more than 10 THz, which covers several to tens of FSRs of the WGM cavity system. Thereby, when we decrease the detuning gradually (equivalent to increasing the pump power), the system could evolve from a 1-FSR FWM-dominant regime to an SRS-dominant regime and then change back to the multi-FSR FWM-dominant regime. As seen in Fig. 7, we observed that, by decreasing the cavity detuning in the simulation, the Kerr comb and Raman comb would appear and disappear by turns. Typically, as the pump power starts to build up in the cavity, Kerr oscillation is first initiated, as displayed in Fig. 7(a). This is a Turing pattern comb with the maximum MI gain at 1-FSR frequency spacing. With further pump detuning, we observe the formation of Raman oscillations as well [Fig. 7(b)], since the Raman gain is larger than the parametric gain. As the pump is tuned further, the occurrence of Stokes and anti-Stokes Raman lines at ∼13 THz on both sides of the pump [Fig. 7(c)] suggest that the Raman gain outperforms the MI gain in this case. Figure 7(d) displays the final detuning step, where a stable 2-FSR Turing pattern Kerr comb is initiated at phase detuning of -5.4×10^{-8}, and the Raman effect diminishes. This simulation result provides another possibility of switching between the Kerr comb and Raman comb state without changing the resonator geometry, which is in accordance with the experimental results in Fig. 5.

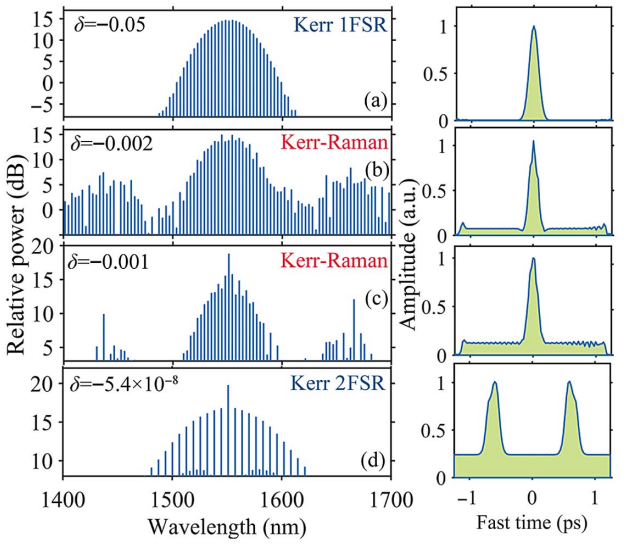

Fig. 7. Simulated spectrum and temporal profile (insets) for generated combs in silica bottle resonators with 402 GHz FSR pumping at 1551 nm for phase detuning of (a) −0.05, (b) −0.002, (c) −0.001, and (d) -5.4×10^{-8} from cold-cavity resonance.

6. DISCUSSION AND CONCLUSION

The 2D Kerr and Raman–Kerr combs presented here provide more degrees of freedom when compared with conventional frequency combs based on fundamental WGMs [5], and the

bottle platform allows for better control of dispersion. Our method is also applicable for any resonator with axial/polar modes. However, the experimental demonstration of wideband 2D frequency combs involving both the axial and azimuthal mode series in a microcavity, although predicted by numerical simulations [33], has proven to be difficult. The first challenge is the much larger mode volume occupied by the bottle resonator. Hence, a higher Raman oscillation threshold is predicted in this case. Second, the axial modes are decoupled, and a large number of spatial overlapped modes are supported in the bottle resonator. This generates numerous avoided mode crossings that impede the formation of solitons in the cavity [34]. We also observed the measured transmission spectra of different resonances overlapping with each other in our experiment. Moreover, matching the axial lines with the azimuthal lines is difficult. Although it could be realized in the surface nanoscale axial photonics (SNAP) platform [35] with a delicate technique, the extremely large mode volume (~10 times larger than the conventional equatorial resonator) as well as the inevitable coupling and interference with the delocalized radiation modes [36] makes the initiation of the combs a great challenge. Therefore, in this work, we propose to exploit the non-degenerate FWM with axial WGMs included for generation of 2D Kerr frequency combs in bottle microresonators. This mechanism overcomes the relatively low MI gain close to the pump frequency similar to the parametric seeding method [37]. With the aid of a simple and convenient fabrication technique, the axial series are brought to match the azimuthal mode series such that the wideband 2D frequency combs are created.

In summary, we have experimentally and theoretically validated an approach for generation of controllable 2D Kerr and Raman–Kerr frequency combs in a high-Q bottle resonator platform. The gain transition between FWM and SRS-dominant states can be achieved in a controllable and reversible way via dispersion management by adjusting the axial coupling position of the microfiber (axial mode q) or axial curvature of the bottle resonator (Δk). In particular, the effect of axial mode number and bottle axial curvature on the GVD couples with each other in the bottle resonator. Notably, broadband 2D Kerr and Raman–Kerr frequency combs with spans of 114 and 242 nm were realized for the first time, to the best of our knowledge, by simultaneous excitation of axial and azimuthal mode sequences ($\mathrm{FSR}_m = 4\mathrm{FSR}_q$). These interesting 2D frequency combs can extend from hundreds to thousands of comb lines with flexible repetition rates and could find applications for future precision spectroscopy and optical clocks in both telecommunication and mid-IR spectral ranges.

Funding. National Natural Science Foundation of China (62005071); Natural Science Foundation of Anhui Province (2008085QF312); Fundamental Research Funds for the Central Universities (JZ2019HGBZ0122, JZ2019HGTA0050); National Key Research and Development Program of China (2019YFE010747).

Acknowledgment. We thank Dr. Rui Niu from the University of Science and Technology of China for helpful discussions.

Disclosures. The authors declare no conflicts of interest.

REFERENCES

1. P. Delhaye, A. Schliesser, O. Arcizet, T. Wilken, R. Holzwarth, and T. J. Kippenberg, "Optical frequency comb generation from a monolithic microresonator," Nature **450**, 1214–1217 (2007).
2. W. Wang, Z. Lu, W. Zhang, S. T. Chu, B. E. Little, L. Wang, X. Xie, M. Liu, Q. Yang, and L. Wang, "Robust soliton crystals in a thermally controlled microresonator," Opt. Lett. **43**, 2002–2005 (2018).
3. Z. Newman, V. N. Maurice, T. Drake, J. R. Stone, T. C. Briles, D. T. Spencer, C. Fredrick, Q. Li, D. A. Westly, and B. Ilic, "Architecture for the photonic integration of an optical atomic clock," Nat. Photonics **6**, 680–685 (2019).
4. Q. Yang, X. Yi, K. Y. Yang, and K. J. Vahala, "Stokes solitons in optical microcavities," Nat. Phys. **13**, 53–57 (2017).
5. G. Lin, S. Diallo, J. M. Dudley, and Y. K. Chembo, "Universal nonlinear scattering in ultra-high Q whispering gallery-mode resonators," Opt. Express **24**, 14880–14894 (2016).
6. M. Yu, Y. Okawachi, R. Cheng, C. Wang, M. Zhang, A. L. Gaeta, and M. Loncar, "Raman lasing and soliton mode-locking in lithium niobate microresonators," Light Sci. Appl. **9**, 1 (2020).
7. Y. Chen, Z. Zhou, C. Zou, Z. Shen, G. Guo, and C. Dong, "Tunable Raman laser in a hollow bottle-like microresonator," Opt. Express **25**, 16879–16887 (2017).
8. Y. Okawachi, M. Yu, V. Venkataraman, P. Latawiec, A. G. Griffith, M. Lipson, M. Loncar, and A. L. Gaeta, "Competition between Raman and Kerr effects in microresonator comb generation," Opt. Lett. **42**, 2786–2789 (2017).
9. S. Fujii, T. Kato, R. Suzuki, A. Hori, and T. Tanabe, "Transition between Kerr comb and stimulated Raman comb in a silica whispering gallery mode microcavity," J. Opt. Soc. Am. B **35**, 100–106 (2018).
10. X. Liu, C. Sun, B. Xiong, L. Wang, J. Wang, Y. Han, Z. Hao, H. Li, Y. Luo, and J. Yan, "Integrated high-Q crystalline AlN microresonators for broadband Kerr and Raman frequency combs," ACS Photon. **5**, 1943–1950 (2018).
11. B. Min, L. Yang, and K. J. Vahala, "Controlled transition between parametric and Raman oscillations in ultrahigh-Q silica toroidal microcavities," Appl. Phys. Lett. **87**, 181109 (2005).
12. Y. Yang, Y. Ooka, R. M. Thompson, J. M. Ward, and S. N. Chormaic, "Degenerate four-wave mixing in a silica hollow bottle-like microresonator," Opt. Lett. **41**, 575–578 (2016).
13. Y. V. Kartashov, M. L. Gorodetsky, A. Kudlinski, and D. V. Skryabin, "Two-dimensional nonlinear modes and frequency combs in bottle microresonators," Opt. Lett. **43**, 2680–2683 (2018).
14. M. Pollinger, D. Oshea, F. Warken, and A. Rauschenbeutel, "Ultrahigh-Q tunable whispering-gallery-mode microresonator," Phys. Rev. Lett. **103**, 053901 (2009).
15. G. S. Murugan, J. S. Wilkinson, and M. N. Zervas, "Selective excitation of whispering gallery modes in a novel bottle microresonator," Opt. Express **17**, 11916–11925 (2009).
16. X. Jin, Y. Dong, K. Wang, and H. Jian, "Selective excitation and probing of axial modes in a microcylindrical resonator for robust filter," IEEE Photon. Technol. Lett. **28**, 1649–1652 (2016).
17. X. Jin, Y. Dong, and K. Wang, "Selective excitation of axial modes in a high-Q microcylindrical resonator for controlled and robust coupling," Appl. Opt. **54**, 8100–8107 (2015).
18. F. Ferdous, H. Miao, D. E. Leaird, K. Srinivasan, J. Wang, L. Chen, L. T. Varghese, and A. M. Weiner, "Spectral line-by-line pulse shaping of on-chip microresonator frequency combs," Nat. Photonics **5**, 770–776 (2011).
19. V. Dvoyrin and M. Sumetsky, "Bottle microresonator broadband and low-repetition-rate frequency comb generator," Opt. Lett. **41**, 5547–5550 (2016).
20. W. Liang, A. A. Savchenkov, Z. Xie, J. F. McMillan, J. Burkhart, V. S. Ilchenko, C. W. Wong, A. B. Matsko, and L. Maleki, "Miniature multioctave light source based on a monolithic microcavity," Optica **2**, 40–47 (2015).

21. D. Farnesi, A. Barucci, G. C. Righini, G. N. Conti, and S. Soria, "Generation of hyper-parametric oscillations in silica microbubbles," Opt. Lett. **40**, 4508–4511 (2015).
22. T. Carmon, L. Yang, and K. J. Vahala, "Dynamical thermal behavior and thermal self-stability of microcavities," Opt. Express **12**, 4742–4750 (2004).
23. G. S. Murugan, M. N. Petrovich, Y. Jung, J. S. Wilkinson, and M. N. Zervas, "Hollow-bottle optical microresonators," Opt. Express **19**, 20773–20784 (2011).
24. J. Riemensberger, K. Hartinger, T. Herr, V. Brasch, R. Holzwarth, and T. J. Kippenberg, "Dispersion engineering of thick high-*Q* silicon nitride ring-resonators via atomic layer deposition," Opt. Express **20**, 27661–27669 (2012).
25. Y. Nakagawa, Y. Mizumoto, T. Kato, T. Kobatake, H. Itobe, Y. Kakinuma, and T. Tanabe, "Dispersion tailoring of a crystalline whispering gallery mode microcavity for a wide-spanning optical Kerr frequency comb," J. Opt. Soc. Am. B **33**, 1913–1920 (2016).
26. F. Shu, P. Zhang, Y. Qian, Z. Wang, S. Wan, C. Zou, G. Guo, and C. Dong, "A mechanically tuned Kerr comb in a dispersion-engineered silica microbubble resonator," Sci. China Phys. Mech. Astron. **63**, 254211 (2020).
27. C. Bao, J. A. Jaramillovillegas, Y. Xuan, D. E. Leaird, M. Qi, and A. M. Weiner, "Observation of Fermi–Pasta–Ulam recurrence induced by breather solitons in an optical microresonator," Phys. Rev. Lett. **117**, 163901 (2016).
28. M. Liu, L. Wang, Q. Sun, S. Li, Z. Ge, Z. Lu, W. Wang, G. Wang, W. Zhang, and X. Hu, "Influences of multiphoton absorption and free-carrier effects on frequency-comb generation in normal dispersion silicon microresonators," Photon. Res. **6**, 238–243 (2018).
29. C. Godey, I. Balakireva, A. Coillet, and Y. K. Chembo, "Stability analysis of the spatiotemporal Lugiato–Lefever model for Kerr optical frequency combs in the anomalous and normal dispersion regimes," Phys. Rev. A **89**, 063814 (2014).
30. Y. K. Chembo, I. S. Grudinin, and N. Yu, "Spatiotemporal dynamics of Kerr–Raman optical frequency combs," Phys. Rev. A **92**, 043818 (2015).
31. H. A. Haus, "Applications of nonlinear fiber optics," Phys. Today **55**, 58–59 (2002).
32. D. Castellolurbe and E. Silvestre, "Comparative analysis of spectral coherence in microresonator frequency combs," Opt. Express **22**, 4678–4691 (2014).
33. S. V. Suchkov, M. Sumetsky, and A. A. Sukhorukov, "Frequency comb generation in SNAP bottle resonators," Opt. Lett. **42**, 2149–2152 (2017).
34. K. E. Webb, M. Erkintalo, S. Coen, and S. G. Murdoch, "Experimental observation of coherent cavity soliton frequency combs in silica microspheres," Opt. Lett. **41**, 4613–4616 (2016).
35. M. Sumetsky and Y. Dulashko, "SNAP: fabrication of long coupled microresonator chains with sub-angstrom precision," Opt. Express **20**, 27896–27901 (2012).
36. X. Jin, K. Wang, Y. Dong, M. Wang, H. Gao, and L. Yu, "Multiple-channel dynamic bandpass filter via radiation modes-assisted transparency in a side-coupled SNAP microcavity," Appl. Phys. Express **12**, 092001 (2019).
37. G. Lin, R. Martinenghi, S. Diallo, K. Saleh, A. Coillet, and Y. K. Chembo, "Spectro-temporal dynamics of Kerr combs with parametric seeding," Appl. Opt. **54**, 2407–2412 (2015).